Smart Mater. Struct. **22** (2013) 025020 (15pp) doi:10.1088/0964-1726/22/2/025020

Dynamic control of a bistable wing under aerodynamic loading

Onur Bilgen[1], **Andres F Arrieta**[2], **Michael I Friswell**[3] **and Peter Hagedorn**[4]

[1] Department of Mechanical and Aerospace Engineering, Old Dominion University, Norfolk, VA 23529, USA
[2] Centre for Structure Technologies, ETH Zurich, Zurich, 8092, Switzerland
[3] College of Engineering, Swansea University, Singleton Park, Swansea, SA2 8PP, UK
[4] Dynamics and Vibrations Group, Technische Universtät Darmstadt, Darmstadt, 64289, Germany

E-mail: obilgen@odu.edu

Received 24 September 2012, in final form 4 December 2012
Published 25 January 2013
Online at stacks.iop.org/SMS/22/025020

Abstract
The aerodynamic evaluation of a dynamic control technique applied to a bistable unsymmetrical cross-ply composite plate with surface bonded piezoelectric actuators is presented. The plate is clamped on one end to form a low-aspect-ratio wing. A previously proposed dynamic control method, utilizing bending resonance in different stable equilibrium positions, is used to induce snap-through between the two equilibrium states. Compared to quasi-static actuation, driving the bistable plate near resonance using surface bonded piezoelectric materials requires, theoretically, a lower peak excitation voltage to achieve snap-through. First, a set of extensive wind tunnel experiments are conducted on the passive bistable wing to understand the change in the dynamic behavior under various aerodynamic conditions. The passive wing demonstrated sufficient bending stiffness to sustain its shape under aerodynamic loading while preserving the desired bistable behavior. Next, by the use of the resonant control technique, the plate is turned into an effectively monostable structure, or alternatively, both stable equilibrium positions can be reached actively from the other stable equilibrium. Dynamic forward and reverse snap-through is demonstrated in the wind tunnel which shows both the effectiveness of the piezoelectric actuation as well as the load carrying capability of both states of the bistable wing.

(Some figures may appear in colour only in the online journal)

1. Introduction

Recently, three review papers have been published on the topic of shape change (morphing) of aircraft by Sofla *et al* [1], by Barbarino *et al* [2] and by Gomez and Garcia [3]. The publication of these reviews in a 2-year period and the continuing developments in materials and electronic systems are indications that morphing in aircraft is becoming more practical and may soon be common in general aviation. An interesting fact is that smooth and continuous aerodynamic control surface designs have been a research interest since the beginning of modern aviation—the first controlled, powered and heavier-than-air flight by the Wright Brothers in 1903. In the context of wing morphing, establishing a wing configuration that is stiff enough to prevent flutter and divergence but compliant enough to allow the range of available motion has been the central challenge in developing a smooth and continuous wing.

Structures capable of adopting two or more statically stable shapes have drawn considerable attention from researchers in the area of control surface design for their potential applications in morphing structures, as no energy is required to hold each of the stable configurations. In certain composite plates, the bistable property appears as a result of residual thermal stresses induced during the curing process due to an unsymmetric stacking sequence (see [4, 5]). The change between stable states is physically realized as a jump phenomenon known as snap-through, which is

 © 2013 IOP Publishing Ltd Printed in the UK & the USA

strongly nonlinear in nature (see [6]). The following sections will briefly summarize a few examples of (1) piezoelectric materials in morphing control surfaces and (2) the use of bistable structures for aerodynamic applications.

1.1. Piezocomposite control surfaces

Significant attention in research has been given to the use of conformal piezoelectric actuators to achieve shape change in variable-camber airfoils. The review article by Barbarino *et al* [2] showed that morphing of camber and twist of the wing using piezoelectric materials resulted in the largest number of wind tunnel and flight tests in aircraft when compared to other morphing categories, such as planform and out-of-plane morphing categories, and also when compared to other actuation sources, such as conventional actuators, shape-memory alloys (SMAs), rubber-muscle actuators and others. In the case of piezoelectric material devices, the rapid development and the reduced cost of small electronics in the last decade has led to several examples of operational small unmanned (and/or remotely piloted) fixed-wing, rotary-wing and ducted-fan aircraft that use smart materials. The following discussion presents a few examples of such aircraft. In 2002, Eggleston *et al* [7] experimented with the use of piezoceramic materials, shape-memory alloys and conventional servomotors in a morphing-wing aircraft. A series of wind tunnel tests showed the feasibility of the smart material systems. Barrett *et al* [8] employed piezoelectric elements along with elastic elements to magnify the control deflections and forces in aerodynamic surfaces. Vos *et al* [9, 10] conducted research to improve the post-buckled-precompression concept for aerodynamic applications. Roll control authority was increased on a 1.4 m span unmanned air vehicle. Kim and Han [11, 12] designed and fabricated a flapping wing by using a graphite–epoxy composite material and a Macro-Fiber Composite (MFC) actuator. A 20% increase in lift was achieved by changing the camber of the wing at different stages of flapping motion.

Bilgen *et al* [13, 14] presented an application for piezocomposite actuators on a 0.76 m wingspan morphing-wing air vehicle. Adequate roll control authority was demonstrated in the wind tunnel as well as in flight. Bilgen *et al* [15, 16] presented static flow vectoring via a MFC actuated thin bimorph variable-camber airfoil and a MFC actuated cascading bimorph variable-camber airfoil. Wind tunnel results and analytical evaluation of the airfoils showed comparable effectiveness to conventional actuation systems and no adverse deformation due to aerodynamic loading. Paradies and Ciresa [17] implemented MFCs as actuators in an active composite wing. A scaled prototype wing was manufactured and models were validated with static and preliminary dynamic tests of the prototype wing. Wickramasinghe *et al* [18] presented the design and verification of a smart wing for an unmanned aerial vehicle. The proposed smart wing structure consisted of a composite spar and ailerons that have bimorph active ribs consisting of MFC actuators. In 2010, Butt *et al* [19, 20] and Bilgen *et al* [21, 22] developed a completely servo-less, wind tunnel and flight tested remotely piloted aircraft. This vehicle became the first fully solid-state piezoelectric material controlled, non-tethered, flight tested fixed-wing aircraft. Ohanian *et al* [23] presented an extensive aerodynamic comparison of a MFC actuated compliant control surface to a servo-actuated conventional control surface for a micro aerial vehicle application.

1.2. Bistable structures

The examples above show the feasibility of piezoelectric materials in small unmanned aircraft; however, in most cases in the literature, the actuator works against an elastic component of the system. In order to maintain a static shape, an actuation force must be maintained against the elastic restoring force. Considering the fact that piezoelectric material actuators have some level of resistive loss associated with them, maintaining static shape requires work to be done on the system. In this context, bistable structures, mainly bistable composite plates, have been proposed to maintain shape without having to do work on the system. Dano and Hyer [24] demonstrated the actuation of bistable composites using SMA wires and MFC actuators under quasi-static loading. The former showed good actuation authority; however, systems incorporating SMAs are difficult to integrate with the bistable composites. Schultz *et al* [25] showed that the MFC actuators were simpler to integrate with the bistable structures; however, snap-through was achieved in only one direction with the use of static excitation. Furthermore, very high voltages were required to drive the MFC actuator even for very compliant [MFC/0/90/MFC] two-ply plates.

Piezoelectric material actuators would be suitable for morphing structures should they show enough authority to induce and reverse snap-through on bistable composite structures. Such structures must also maintain rigidity in order to be a useful passive load carrying aerodynamic surface. Bistable structures have been applied to aerodynamic applications by several researchers. Mattioni *et al* [26–28] and Diaconu *et al* [29, 30] showed the application of bistable composite structures to aerodynamic applications. Daynes *et al* [31] used a layered bistable plate structure for a trailing flap demonstrator. Recently, Arrieta *et al* [32] and Senba *et al* [33] proposed and demonstrated the idea to exploit the rich dynamics of bistable composites to enhance the effectiveness of actuation. In the case of Arrieta *et al* [32] the morphing strategy was based on the possibility of using external energy from dynamic perturbations on the structure to enhance the authority of a MFC actuator targeting a sub-harmonic resonance of a bistable composite plate, resulting in dynamically triggered snap-through. However, due to symmetric dynamics of the tested plate and lack of authority of the MFC actuator, no reversed snap-through was achieved for the $[0_2/90_2]$ plate. Senba *et al* [33] achieved a dynamically triggered reversed snap-through on a $[0/45/\mathrm{MFC}^{45}]$ plate of dimensions 148 mm × 148 mm using a MFC M8557-P1 actuator bonded on the surface with the aid of an added mass approximately equivalent to 100% of

that of the tested laminate. It is important to note that the degree of bistability of $[0_n/45_n]$ composites is much smaller than that achieved with a cross-ply $[0_n/90_n]$ lay-up, hence the achievable elastic deformation is greater for the latter type. The added mass increases the effectiveness of dynamic actuation; however, the large weight added to the structure is clearly not desirable in morphing structures for aerodynamic applications.

The brief literature review above shows the merits of exploiting the nonlinear response and dynamic perturbations of a bistable composite structure as a morphing strategy. Furthermore, it is well known that for structures which have multiple configurations, such as arches and shells, the load triggering the instability leading to a jump to another stable state is reduced when using dynamic forcing in comparison to static actuation (see [34]). The key to exploiting the nonlinear dynamic response of such structures is the ability to predict important linear dynamic features such as natural frequencies and mode shapes in different stable states. Some studies of such dynamic characteristics for an unconstrained bistable composite can be found in the literature (see [35, 36]).

As with any active or semi-active compliant aerodynamic surface, a bistable piezocomposite wing is practical if one achieves (1) sufficient aerodynamic load carrying capability in each state and (2) bi-directional snap-through using relatively low excitation voltages. Such structures can be realized by careful selection of actuator placement, boundary conditions and laminate lay-up. In this context, Arrieta *et al* [37–39] presented the modeling, implementation and demonstration of purely piezoelectric material induced dynamic forward and reverse snap-through of a bistable unsymmetric composite plate with a clamped edge. The motivation for the current paper is to demonstrate a similar piezoelectric material induced dynamic behavior in the presence of aerodynamic loading for possible employment of the bistable plate in aerodynamic control surfaces. Section 2 presents the motivation for the current research. Next, the design of the bistable composite wing is presented, including composite lay-up sequence and actuator placement. Finally the wind tunnel experiments on the bistable wing are presented and compared to a baseline flat plate aluminum wing. The paper concludes with a brief summary of results.

2. Resonant control technique

In general, morphing wing structures achieve shape change in a unique fashion; however, some concepts, more specifically the ones employing conformal piezoelectric materials, may not produce similar aerodynamic effects when compared to conventional wing structures. In general, the main purpose of employing piezoelectric materials is to increase aerodynamic efficiency by achieving surface continuity and by reducing the number of parts and mass concentrations. Since most piezoelectric materials are limited in their strain output, these materials are typically not proposed to achieve relatively large shape changes that allow an aircraft to operate in a wide range of fluid conditions. Coupled with compliant structures, piezocomposite wings inherently have elastic restoring forces and they are limited in their deformation. Both of these properties simultaneously create advantages and disadvantages for a piezocomposite wing compared to a semi-rigid wing with discrete control surfaces.

In contrast to a monostable piezocomposite wing, a bistable, or a multi-stable, piezocomposite wing structure may have (1) desired compliancy, (2) large deformation output and (3) maintain deformation with zero energy consumption. Recent research by Arrieta *et al* [37, 39] presented the modeling of the nonlinear dynamic behavior of a cantilevered bistable composite plate actuated with piezoelectric elements and demonstrated dynamic forward and reverse snap-through. The cantilever boundary condition is achieved by tailoring the lay-up of the composite laminate, as demonstrated previously by Mattioni *et al* [26–28], allowing the resulting bistable specimen to be connected to the rest of the wing structure or to a vehicle directly. The modeling is based on the assumption that the snap-through mechanism is governed by a deflection threshold dependent on the stable geometries of the composite defined as a critical displacement. As a result, the geometry of each stable state can be assumed allowing the calculation of natural frequencies and mode shapes by solving the associated linear vibration problem using a Ritz approach. The results obtained from the linear vibration problem, in particular the calculated eigenfunctions, are used to obtain a low order nonlinear model. The obtained low order model allows the investigation of the snap-through behavior and cross-well oscillations exhibited by the multi-stable system. The model is used to inspect the spacing between the frequencies of the first snap-through modes associated with each state. It is shown that the separation between the modal frequencies is of key importance in order to avoid complex cross-well dynamics leading to chaotic oscillations when triggering snap-through. The parameter space for the actuation input in terms of voltage amplitude and forcing frequency is initially investigated theoretically, revealing the lowest required voltage to trigger snap-through for each stable configuration. The presented model is used to design the optimal configuration control of a cantilevered bistable composite.

The proposed control technique is very simple in principle. The bistable structure is harmonically excited using the surface bonded piezoelectric materials. By targeting distinct operating frequencies, mainly close to the resonance of each state, the apparent stiffness of the composite plate is dynamically reduced (for that state) which in return enables 'forward' snap-through at low peak excitation voltages applied to the piezoelectric material. This excitation voltage is lower for dynamic actuation compared to the quasi-static actuation case. Once the snap-through occurs, the structure maintains its position in that state even if the excitation is still applied. A similar method is followed to go back to the original state. By targeting the resonance of the 'second' state, the stiffness is dynamically reduced and 'reverse' snap-through is induced. In both actuation cycles, once the state changes, the effective bending stiffness is modified and hence the resonance frequency associated with the stable equilibrium is also changed. An excitation, at a distinct frequency, that causes resonance in one state no longer results

in resonance in the other given that the frequencies are sufficiently separated. This automatic control behavior avoids undesirable continuous forward and reverse snap-through for a distinct excitation frequency.

Following the modeling work, Arrieta *et al* [37, 38] demonstrated the control technique on a rectangular, cantilevered, bistable, unsymmetric cross-ply piezocomposite plate. The plate is actuated with two MFC M8557-P1 type actuators bonded on the surface near the clamped boundary. First, the full linear and low order nonlinear models are compared to experimental results showing a good match with the observed behavior. In particular, the first bending mode of each stable state, associated with minimum actuation snap-through modes, is accurately matched for a number of different multi-stable specimens. The experiments demonstrated controlled snap-through between each state at relatively low-voltage amplitudes in comparison to statically actuated bistable composites. An experimental parametric investigation revealed the lowest voltages required to induce forward and reverse snap-through. Complemented by the theoretical modeling, previous works by the authors have shown that reversible dynamic snap-through can be achieved on bistable composite plates using only surface bonded piezoelectric actuators. Inertial augmentation of dynamic excitation has been shown to be the key in transitioning between the two static equilibrium positions.

In the current research, the reason for employing piezoelectric materials is to achieve a similar aerodynamic function as conventional control surfaces while reducing the number of discrete surfaces, discontinuities and parts. In return, such a concept is likely to reduce maintenance and fabrication costs, and reduce the weight of the overall aerodynamic surface; however, the analysis of these desired features is beyond the scope of the current research. Here, attention is directed to the characterization of fundamental aerodynamic performance, quantified in terms of lift coefficient, drag coefficient and lift-to-drag ratio.

3. Design of the bistable piezocomposite wing

A partially active unsymmetrical cross-ply laminate is designed to be bistable by locking-in residual stresses during the elevated-temperature curing process. The composite plate consists of two separate stacking sequences. A large portion of the plate is formed using an unsymmetrical $[0_2/90_2]$ sequence. A much smaller portion is designated as the clamped base and it has a symmetrical $[0/90_2/0]$ sequence. A carbon fiber-epoxy prepreg, type E022-T700 manufactured by SLG [40], is used for each layer. Figure 1 illustrates the laminate sequence of the original rectangular composite plate.

The laminate is cured at elevated temperature. Cooling down to room temperature results in bistable behavior due to the stresses that are locked in due to the elevated temperatures. The rectangular plate is cut in to a tapered planform with a taper ratio of 0.73. The leading-edge (LE) is swept back at an angle of 13.8°. A base airfoil is used to serve as an aerodynamically shaped clamping mechanism for the base of

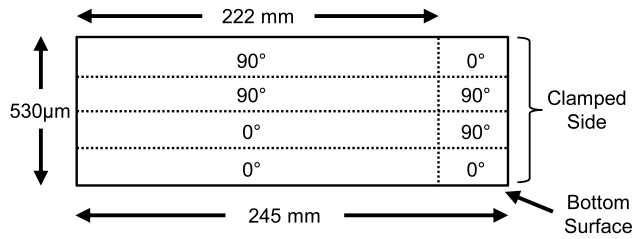

Figure 1. Stacking sequence of the bistable unsymmetrical cross-ply laminate. The illustration is not proportional to actual dimensions.

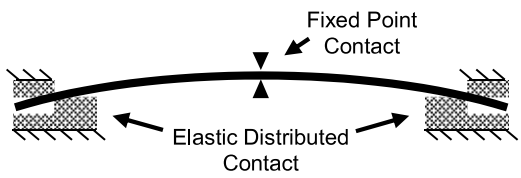

Figure 2. An illustration of the boundary conditions near the clamped base of the bistable laminate.

the bistable plate. The clamped side of the bistable plate and the boundary conditions are illustrated in figure 2.

As shown in the illustration, the side boundary conditions which correspond to the LE and trailing-edge (TE) of the root section are achieved by clamping the bistable plate between two elastic rubber pads. These pads are arranged so that the clamped boundary roughly follows the root curvature of the free bistable plate. In addition, a middle boundary condition is introduced which corresponds to the mid-chord of the root section. This middle boundary is achieved by two collinear screws, roughly 3 mm in diameter, which can be adjusted to fix the position of the mid-chord of the root of the plate in a desired condition. By changing the root curvature of the bistable plate, one can change the relative depth of the potential wells, and therefore change the maximum aerodynamic load carrying capability in each state of equilibrium. In the current examination, the authors used this mechanical adjustment to fine tune the bistable behavior. Such mechanical adjustment is found to be both necessary and useful because the energy density of the actuation source, the MFC actuator in this case, is limited. Relative to the free curvature of the plate, if one increases the curvature through the use of the middle boundary, *State 1* is strengthened. In this paper, *State 1* is defined as the *stiff* state and it has a major curvature mainly along the chord axis. The effect of curvature in *State 1* is analogous to the effect of camber. In contrast, if one decreases the curvature of the clamped root section with the use of the middle boundary, *State 1* is weakened and *State 2* is strengthened. *State 2* is defined as the *compliant* state and it has a major curvature mainly along the span axis. The effect of curvature in *State 2* is analogous to the effect of dihedral. Figure 3 illustrates the planform view of the bistable wing clamped on the base airfoil.

The base airfoil has a NACA 0012 profile and it consists of two sections. The upper section, adjacent to the root of the complete wing, is a solid steel NACA 0012 airfoil with a 254 mm chord. The lower section, adjacent to the root

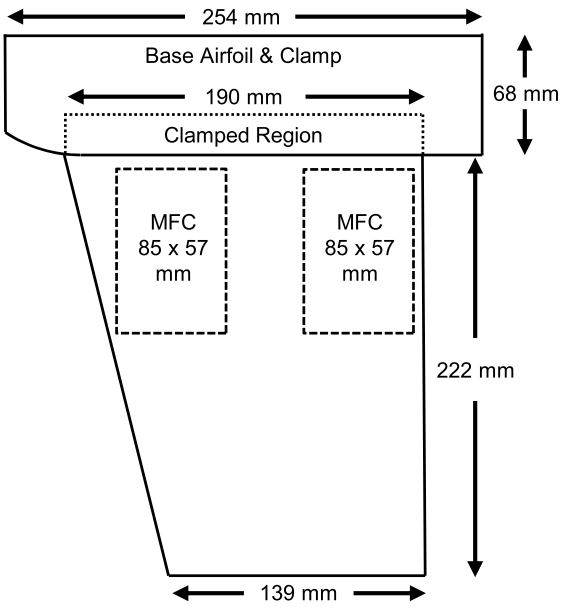

Figure 3. Planform illustration of the bistable wing clamped on the base airfoil. The figure illustrates the actual proportions of the geometric features.

of the bistable plate, is a multi-part clamping mechanism; however, it also has a NACA 0012 profile in two planes. The base has three major functions. The first function is to transfer the aerodynamic loads to the moment arm of the wind tunnel load balance system (described later). Second is to create the desired boundary conditions to the bistable piezocomposite wing. Its third function is, by the use of the steel upper section, to add inertia to the base of the bistable plate so that the boundary, dynamically, behaves similarly to a fuselage or a main wing where the bistable wing would be attached in reality. Figure 4 shows a picture of the bistable piezocomposite wing clamped to the base airfoil.

A MFC actuator is used to excite the bistable plate. The MFC actuator was originally developed at NASA Langley Research Center [41, 42] and offers structural flexibility and high actuation authority. The in-plane poling and subsequent voltage actuation allows the MFC to utilize the *33* piezoelectric effect, which is higher than the *31* effect used by traditional piezoceramic actuators with through-the-thickness poling [43]. Two MFC M8557-P1 type actuators are bonded near the base of the bistable plate on the lower 'pressure' surface of the wing. As shown in figure 1, the fibers on the lower surfaces are oriented at 0° which corresponds to the span axis. In order to maximize the out-of-plane bending induced by the MFC actuator, the piezoceramic fibers of the MFC must be close to the effective neutral plane of the unsymmetric cross-ply laminate and the plate must be compliant in bending and stiff in in-plane extension. An analysis of thin MFC actuated structures is presented in Bilgen *et al* [44] and the results from that analysis are used to aid the design in the current research. In the case studied here, the out-of-plane deflection induced on the bistable plate by the unidirectional in-plane actuation of the MFC actuator is maximized by bonding the MFC actuator directly on the lower layer with 0° (spanwise) fiber orientation.

The complete wing structure which consists of the base airfoil and the bistable wing has a span of 290 mm. The tip chord is 139 mm and the root chord is 254 mm. The mean aerodynamic chord is 185 mm. As noted earlier, the base airfoil has a NACA 0012 profile. The geometric features of the wetted bistable wing are presented in table 1. The term *laser-line* in table 1 indicates the spanwise location where the laser displacement sensor is used to measure the shape of the wing along the chordwise direction. This line is approximately 143 mm from the root of the complete wing structure.

4. Wind tunnel experiments

This section presents the experimental examination of the structural and aerodynamic behavior of the bistable piezocomposite wing. First, the wind tunnel setup is introduced. Next, the passive aerodynamic characteristics of

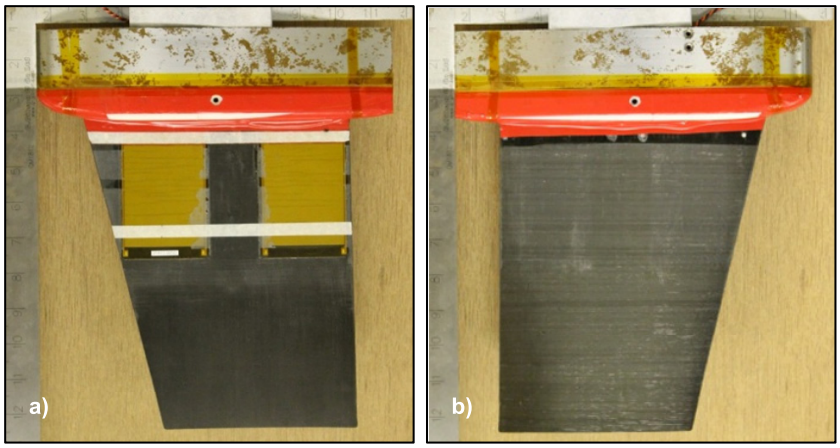

Figure 4. Lower (a) and upper (b) surfaces of the bistable wing with base airfoil. There are two strips of off-white masking tape along the chordwise direction which are used to aid reflectivity for laser displacement measurements.

Table 1. Geometric properties of the wetted area of the bistable piezocomposite wing in two different stable equilibria.

State	Designation	Span location (mm)	Chord (mm)	Camber (% chord)
1	Root	68	190	1.8
	Laser-line	143	171	2.1
	Mid-span	175	163	2.2
	Tip	290	139	2.9
2	Root	68	190	1.6
	Laser-line	143	171	0.3
	Mid-span	175	163	0.0
	Tip	290	139	0.7

the bistable wing are presented. Finally, in this section, the active aerodynamic response of the wing is shown.

4.1. Wind tunnel setup

Aerodynamic experiments were conducted in a low speed, open circuit and closed test section wind tunnel facility which is capable of reaching a freestream velocity of 28 m s^{-1}. At the inlet, an aluminum honeycomb flow-straightener and a fiberglass mesh are used to condition the flow. After the converging nozzle, the test section has a 610 mm × 610 mm (24″ × 24″) octagonal cross section. The test section is converted to a 610 mm × 381 mm (24″ × 15″) semi-octagonal cross section by the use of a removable splitter plate. The wind tunnel fan is driven by a motor and the speed is electronically controlled. The test specimen can be rotated in the test section about its pitch axis by the use of a motor-driven rotary stage. A six-component load cell and a strain-gage amplifier, models MC3A-100 and MSA-6 manufactured by AMTI Inc., are used to acquire forces and moments in three axes simultaneously. The flow velocity and temperature are electronically monitored. Flow velocity during the tests is observed using four static ports at the inlet of the test section, 1.21 m upstream of the quarter-chord of the airfoil, and an Omega PX653 type pressure transducer. The temperature of the flow is measured using a thermocouple and an Omega CCT series amplifier and conditioner, and recorded for each run. The test section is configured for a semi-span experiment using a splitter plate as shown in figure 5.

The quarter-chord of the airfoil is located at 356 mm from the beginning of the splitter plate along the streamwise direction. The span axis is oriented normal to floor of the test section (and ground). The balance assembly mainly consists of the load cell and the rotary table. The sting is mounted to the rotary table and it supports the test specimen without contacting the tunnel walls. The test section between the upper splitter plate and the lower tunnel wall is 381 mm tall and there is a roughly 1–2 mm gap between the root of the wing and the splitter plate. Mueller and Burns [45] showed that gap sizes around 0.5% of the span are usually acceptable and do not affect the results. For the semi-span specimens tested here, the maximum gap height is 0.7%. Although the gap dimension is small, the percentage is still higher than recommended because of the small span of the specimens.

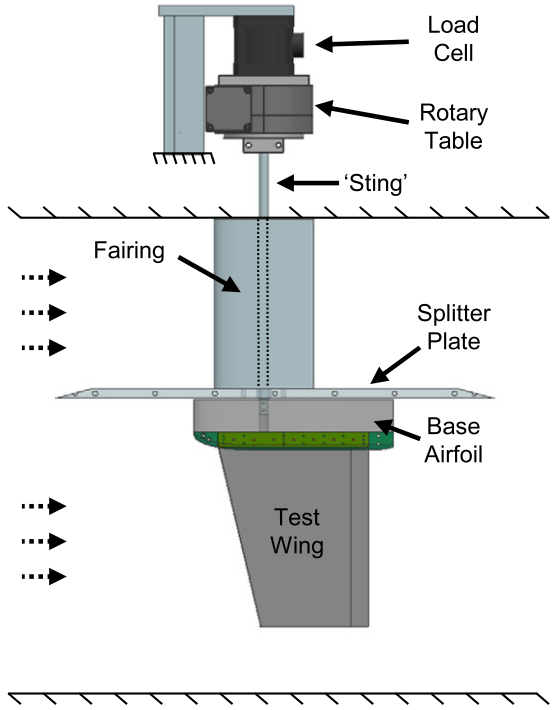

Figure 5. The wind tunnel setup showing an illustration of the load balance and the complete wing structure. The upper and lower walls of the test section and the fairing around the sting are also shown.

The displacement measurements are conducted at the quarter-chord location and at 100 mm from the quarter-chord along the *laser-line* which is located 143 mm from the root of the complete wing structure. The displacement is measured using a MTI LTC-300-200-SA laser displacement sensor with ±20 μm resolution, mounted on the side wall of the test section on a stepper-motor-controlled linear stage. In addition, three control channels are designated for controlling various parameters on the specimen. Two of the channels are used to control the voltages to the two MFC actuators on the bistable piezocomposite wing. Both control signals are amplified and buffered using a TREK 2220 high-voltage amplifier with 200 V/V gain. All parameters are controlled and measured automatically with a National Instruments (NI) cDAQ data acquisition system and a personal computer. A total of 16 channels are monitored using four NI 9239 four-channel, isolated, 24-bit voltage input cards. The output signals are generated using two NI 9263 16-bit, four-channel voltage output cards. For each test point, a 10 s data block is sampled at 100 Hz and then averaged to get the mean value for each measurement of interest.

The streamwise turbulence of the flow in the empty test section is measured by a standard hot wire anemometry technique. A Dantec 55P16 type probe is used along with a Dantec miniCTA bridge amplifier. The probe is placed at the center of the test section (aligned approximately at the quarter-chord location along the streamwise direction) for all turbulence tests. The signal is conditioned with a Kemo VBF/24 type elliptic filter. After proper conversion of the measured voltages to velocity (V), the turbulence intensity

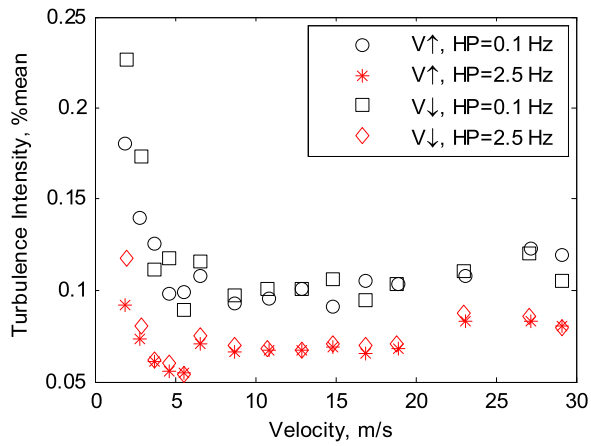

Figure 6. Turbulence intensity versus velocity at the center of the empty test section. The low-pass filter is set to 10 kHz.

(*TI*) is calculated by

$$TI = \frac{V_{\mathrm{rms}}}{V_{\mathrm{mean}}} \times 100,$$

$$\text{where } V_{\mathrm{rms}} = \sqrt{\frac{1}{n}\sum_{i=1}^{n}(V_i - V_{\mathrm{mean}})^2} \tag{1}$$

where the index i represents each sample. Turbulence intensity is measured at several velocities for different filter settings. The presentation of turbulence for different bandwidths is commonly used in the literature [46] to show the frequency components of the turbulence. Figure 6 presents turbulence intensity for two different high-pass (HP) filter settings and for up and down sweep of the velocity.

The effect of the high-pass filter is significant, and as expected, the turbulence intensity appears to decrease as more of the low frequency content of the signal is filtered. The lowest turbulence is observed at around 5 m s^{-1} and the highest around the lower range of the wind tunnel. In summary, an average 0.1% turbulence intensity is derived from 0.1 Hz to 10 kHz band-pass filtered signal for the current test speed range of 5–20 m s^{-1}. The turbulence of the wind tunnel used in this paper is comparable to other tunnels used in the research area.

Barlow [47] suggests several wind tunnel corrections due to the existence of the walls around the wing, the buoyancy caused by the longitudinal pressure gradient and the development of the boundary layer along the walls. The solid blockage term, ϵ_{sb}, and the wake blockage term, ϵ_{wb}, which are described in Barlow [47], can be calculated relatively accurately for conventional wings. Since the specimen in discussion has a non-conventional geometry, the effects of the wind tunnel wall and buoyancy corrections are neglected to maintain the validity of absolute values of the reported coefficients. The reported lift and drag coefficients, C_{l} and C_{d}, are assumed to be equal to the uncorrected lift and drag coefficients, C_{lu} and C_{du}, which are calculated by

$$C_{\mathrm{l}} = C_{\mathrm{lu}} = F_{\mathrm{lift}}/(0.5\rho c b_{\mathrm{r}} v_{\mathrm{qc}}^2), \tag{2}$$

$$C_{\mathrm{d}} = C_{\mathrm{du}} = F_{\mathrm{drag}}/(0.5\rho c b_{\mathrm{r}} v_{\mathrm{qc}}^2) \tag{3}$$

where F_{lift} and F_{drag} are the measured lift and drag forces, ρ is the density of air, c is the mean aerodynamic chord, b_{r} is the reduced semi-span (due to boundary layer displacement thickness) and v_{qc} is the flow speed calculated at the quarter-chord location. Note that density is calculated using the relatively fixed absolute pressure measured in the lab and the temperature of the flow which is recorded during each test.

The flow velocity and reduction in span are calculated as follows: first, a calibration test is conducted in the empty test section between the static ports (sufficiently upstream of the airfoil location) and the Pitot-static tube located at different locations along the flow axis. The velocity is measured with the Pitot-static tube at each location, and the development of a boundary layer (BL) is calculated by applying Bernoulli's equation and conservation of mass. From Fox [48], the BL displacement thickness (from the calibration experiment) is calculated approximately as 1.2 mm. Since there is a gap of maximum 2 mm between the splitter plate and the root of the wing, no reduction in span is applied due to the boundary layer. The flow velocity during aerodynamic tests is calculated by applying the calibration described above, between the static-port and the Pitot-static tube a quarter-chord location, to the static-port measurement which is recorded at each test point.

The experimental measurements are prone to the relative errors induced by the uncertainty in setting the pitch angle, the flexibility in the balance system and the nonlinearity in the load cell. The absolute values have uncertainties due to several parameters such as air density and flow velocity measurements. The uncertainty analysis of each measurement is conducted by following the AIAA Standard [49].

4.2. Flat plate wing baseline aerodynamic response

A flat plate wing is tested for its fundamental aerodynamic characteristics as a baseline to the bistable piezocomposite wing. This flat plate wing is practically equivalent to the bistable wing in terms of planform and the same base airfoil is used for clamping and attachment purposes. The span is 292 mm and the mean aerodynamic chord is 185 mm. The complete wing structure is theoretically symmetric, although a small amount of asymmetry exists due to tolerance limitations caused by the manufacturing and assembly processes. The flat plate wing is made of 2.95 mm thick aluminum and its deformation under aerodynamic loading is negligible. The LE has a radius of approximately 1.48 mm and the TE is tapered to form a sharp edge. The wing is shown in figure 7.

A set of aerodynamic measurements are conducted on the flat plate wing. Figures 8(a) and (b) present the experimental three-dimensional (3D) lift and drag coefficients at three different flow velocities. Figure 8(a) also presents the theoretical two-dimensional (2D) infinite-span and the 3D finite-span lift curves for reference. An aspect ratio (AR) of 1.6 is assumed for the planform of both the baseline and the bistable wings (attached to the base airfoil). Figure 8(b) presents the induced drag for a 3D wing which is derived from the theoretical lift curve presented in figure 8(a). The angle-of-attack is calculated by fitting a known flat plate

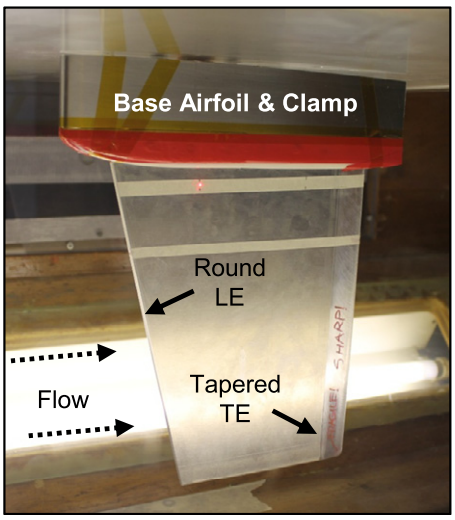

Figure 7. Baseline aluminum flat plate wing and the base airfoil installed in the test section.

profile to the two points, 100 mm apart in the chordwise direction, measured by the laser displacement sensor along the laser-line. As noted in table 1, the laser-line is approximately 143 mm from the root of the complete wing structure.

The experimental lift and drag measurements are close to the theoretical predictions for a finite-span wing. This observation is important because it establishes confidence in the conclusions derived from the measurements. In figure 8(a), a non-zero lift coefficient at the zero degree angle of attack (AOA) indicates that there is a fixed AOA offset which has two main causes. First, there is a small error in deriving the AOA from the laser displacement measurements. Second, the complete wing structure has small asymmetry due to its overall geometry and its surface characteristics, and therefore a non-zero lift is observed at a 0° AOA. Similar conclusions can be derived from the experimental drag response, which is presented in figure 8(b). In summary, both the lift and drag coefficient measurements are as expected; however, the absolute value of the AOA should be treated carefully as this geometric parameter is difficult to measure accurately for the specimens considered in this paper. In contrast, the change in AOA induced by the rotary table and the change derived using the laser displacement measurements are virtually equivalent.

4.3. Bistable wing aerodynamic response—control off

The bistable wing clamped to the base airfoil is evaluated for its fundamental aerodynamic characteristics. As noted earlier, the span is 290 mm and the mean aerodynamic chord is 185 mm. A detailed description is presented in section 3. Figure 9 shows the bistable wing in the test section. In *State 1*, the wing is cambered; however, dihedral is nearly zero. There is a very small amount of twist. In *State 2*, the wing has a nearly symmetric profile; however, a significant amount of dihedral is clearly visible.

Figure 9(a) shows the lower surface of the bistable wing in *State 1* which is referred to as the stiff state—its 'resonance frequency' about the stable equilibrium position is higher when compared to the other state. Figure 9(b) shows the lower surface of the same bistable wing; however, in *State 2*, which is referred to as the compliant state, its 'resonance frequency' about the stable equilibrium point is lower when compared to the other state. Frequency response measurements about the two stable equilibria are presented later.

The first aerodynamic measurement on the bistable wing is conducted to understand the natural (passively induced) snap-through that is caused by an 'adverse' pressure gradient induced on the structure as a result of freestream. A set of AOA sweeps are conducted in the range of 10–20 m s^{-1} nominal velocity values—the velocity range is swept in 2.5 m s^{-1} steps. The AOA sweep is conducted, in both directions, in the range of −20° to +20°—the AOA range is swept in 0.5° steps. The main reason for varying the freestream velocity and the AOA is to simulate the working environment for such a structure. More precisely, the distribution of the pressure is simulated mainly by varying

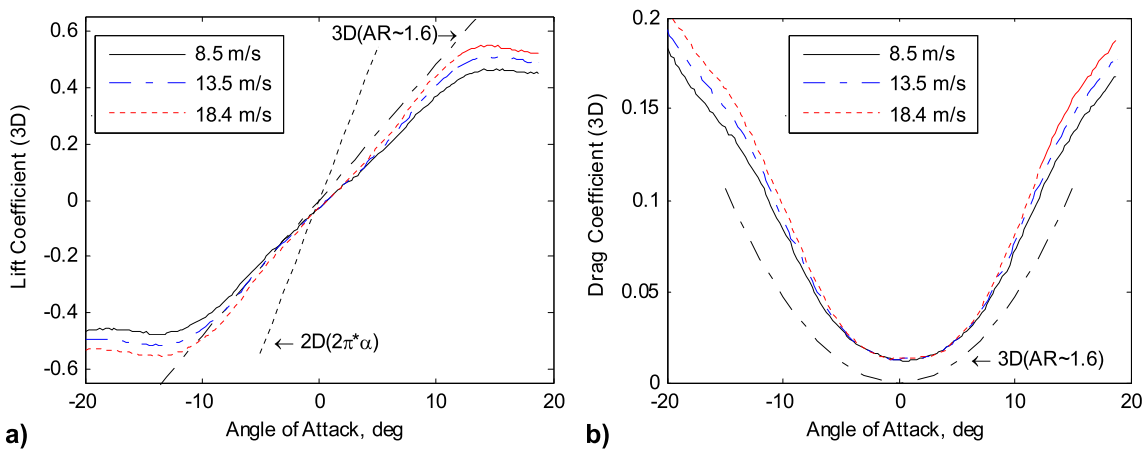

Figure 8. Experimental 3D (a) lift and (b) drag coefficients for the flat plate wing clamped on the base airfoil in response to AOA and freestream velocity. $Re_{\mathrm{MAC}} = 104\,000$, 165 000 and 225 000.

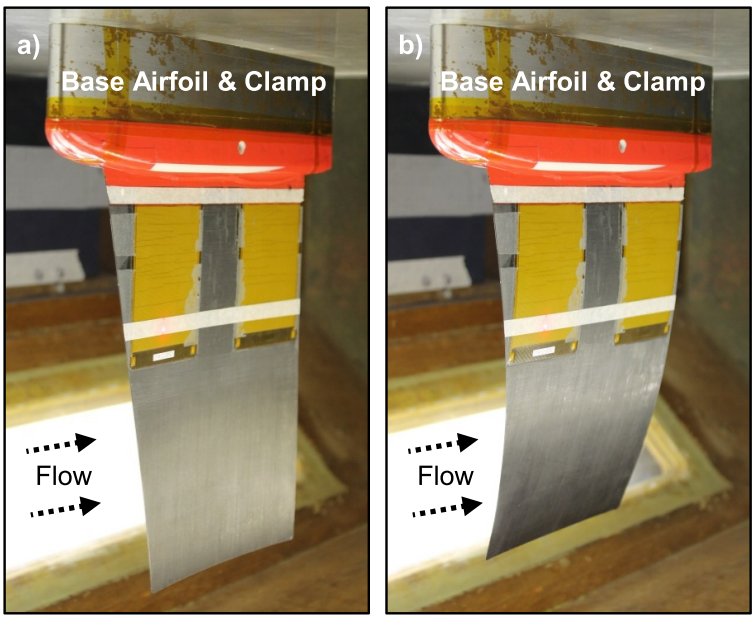

Figure 9. The bistable wing clamped on the base airfoil and mounted in the test section. Two MFC M-8557-P1 type actuators are bonded to the lower surface of the bistable wing.

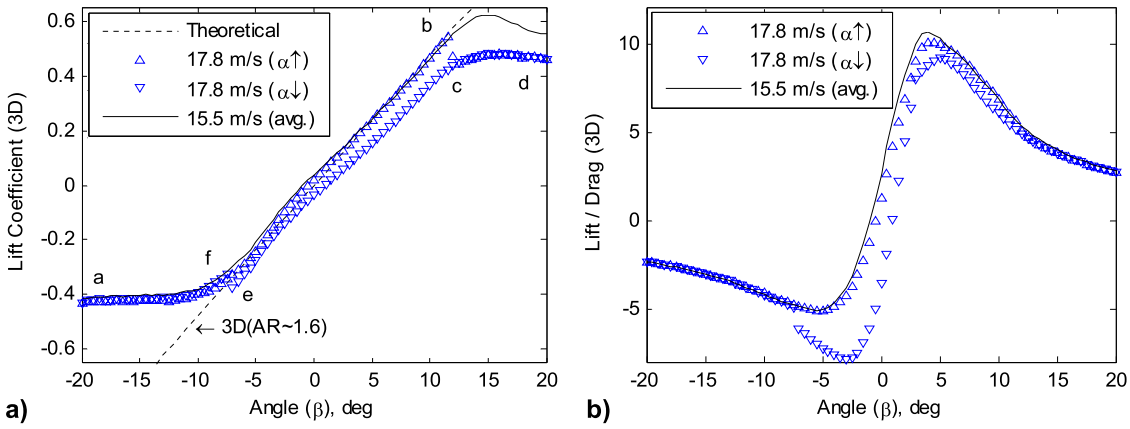

Figure 10. Experimental (3D) aerodynamic response of the passive bistable wing to rotation angle sweep (up–down) and freestream velocity: (a) lift coefficient, (b) lift-to-drag ratio. $Re_{\mathrm{MAC}} = 189\,000$ and $218\,000$.

the AOA and the net pressure acting on the wing is mainly simulated by varying the freestream velocity. The first goal is to demonstrate the fact that the structure can sustain a certain level of adverse pressure gradient without snapping to another state. This property, if demonstrated, shows the passive load carrying capability. The critical values of snap-inducing velocity and AOA are key values in determining the passive load carrying capability.

First, the critical values that induce snap from *State 1* to *State 2* are examined. Next, a fixed velocity is selected. The AOA is started at $-20°$ where the pressure gradient is favorable to *State 1*; further increase in the magnitude (e.g. AOA $< -20°$) does not induce snap-through to *State 2*. The AOA is incremented in 0.5° steps. As the AOA is increased, the favorable pressure gradient to *State 1* switches, at an unknown value, to the adverse pressure gradient to *State 1*. The pressure gradient becomes favorable to *State 2*. Further increase in the AOA may cause the adverse pressure gradient to induce snap-through from *State 1* to *State 2* at a critical AOA value. The cycle is reversed when starting the AOA at $+20°$ and reducing it to $-20°$. The snap-through may occur if the net pressure, primarily controlled by the freestream velocity, is high enough in the AOA range that is examined; therefore a critical freestream velocity also exists for a preselected range of AOA. Below the critical freestream velocity, a state can be passively held for the entire AOA range that is of interest. Snap-through is induced by the dynamic pressure if the critical velocity is exceeded.

Figure 10 presents the aerodynamic response of the bistable plate at two different freestream velocities where the AOA is first swept up from $-20°$ to $+20°$ and swept back down to $-20°$. The wing is set at *State 1* which is the favorable state at $-20°$ AOA. As noted above, five velocity values are examined; however, only the two important velocity values

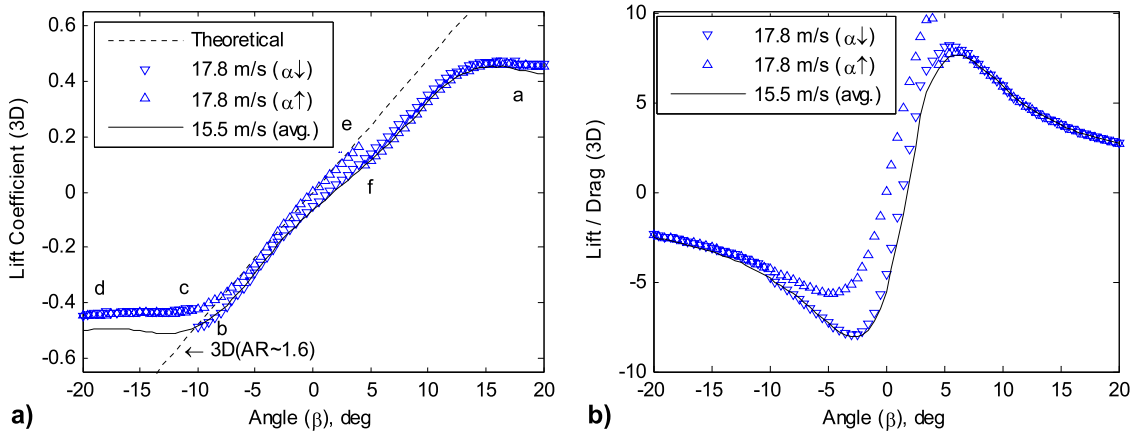

Figure 11. Experimental (3D) aerodynamic response of the passive bistable wing to rotation angle sweep (down–up) and freestream velocity: (a) lift coefficient, (b) lift-to-drag ratio. $Re_{\mathrm{MAC}} = 189\,000$ and $218\,000$.

are presented. It should be noted that the independent variable for the pitch angle is selected as the angle determined by the rotary table since the calculation of the geometric AOA of the 3D structure in the wind tunnel is impractical with the available sensors. Figure 10 also presents the theoretical finite-wing lift curve for reference and to aid comparison to the flat plate response.

A snap-through is not observed for the complete AOA range, in both directions, at 15.5 m s^{-1} and all other velocities below this critical value. Due to the lack of aerodynamic hysteresis, the AOA up and down sweeps are averaged and presented as a single curve for the 15.5 m s^{-1} velocity test. In contrast, at 17.8 m s^{-1}, snap-through is observed in both directions as expected—indicating that the critical velocity value is in the range of 15.5–17.8 m s^{-1}. The path *abcdefa* is indicated in the figures to aid the discussion.

Similar to the discussion above, figure 11 presents the aerodynamic response of the bistable plate at two different freestream velocities where the AOA is first swept down from +20° to −20° and swept back up to +20°. The wing is set at *State 2* which is the favorable state at +20° AOA.

The response for the AOA down–up sweep is very similar to the previously presented AOA up–down sweep. A snap-through is not observed for the complete AOA range, in both directions, at 15.5 m s^{-1} and all other velocities below this critical value. Due to the lack of aerodynamic hysteresis, the AOA up and down sweeps are averaged and presented as a single curve for the 15.5 m s^{-1} velocity test. In contrast, at 17.8 m s^{-1} snap-through is observed in both direction as expected—indicating that the critical velocity value is in the range of 15.5–17.8 m s^{-1}.

An important detail is that all of the wind tunnel tests on the bistable wing are conducted without removing the specimen and without changing its mounting angle with respect to the rotary table. This consistency between different tests allows for a fair comparison and allows certain conclusions to be made regarding the load carrying capability and the snap-through behavior.

4.4. Frequency response of the bistable wing without aerodynamic loading—control on

Section 4.3 described the passive behavior of the bistable piezocomposite in the presence of realistic aerodynamic loading conditions. As described before, the purpose of this paper is to demonstrate dynamic forward and reverse snap-through in the presence of aerodynamic loading. The most effective method for dynamically inducing snap-through is to use the resonant behavior of the structure. Therefore a frequency response analysis is conducted about both stable equilibrium positions. In this section, a preliminary wind-off analysis is conducted to examine the dynamic behavior of the wing while it is mounted on the wind tunnel balance.

An LTC-300-200-SA laser displacement sensor and a Siglab 20–22 frequency analyzer is used to measure the single-point displacement of the complete wing structure mounted in the wind tunnel as previously illustrated in figure 5 and shown in figure 9. A chirp signal is used for the frequency response function (FRF) measurements, where the excitation is a sine tone with continuously varying frequency in a selected frequency range. The control signal to the MFC actuators is amplified using the TREK 2220 high-voltage amplifier. The experiments are conducted at a single excitation voltage level of 200 V_{ac} which is assumed to be in the linear actuation regime. Figure 12 presents the tip-displacement to harmonic-excitation FRF comparison of the MFC actuated bistable wing in *States 1* and *2*. The experimental results presented in figure 12 correspond to the different DC offset levels where the DC offset is used to actively change the mean spanwise curvature of the wing and therefore change the effective stiffness about the stable equilibrium positions.

Figure 12(a) presents the frequency response around the first bending resonance of the wing when it is in *State 1* which is designated as the stiff state. The first bending resonance is observed around 30.9 Hz for the bistable plate in *State 1* and excited with a −250 V_{dc} offset. Resonance frequencies for 0 V_{dc} and +250 V_{dc} are observed around 30.7 and 30.3 Hz, respectively. Note that a DC offset above +500 V_{dc} causes transition to *State 2* and in fact turns the bistable wing into

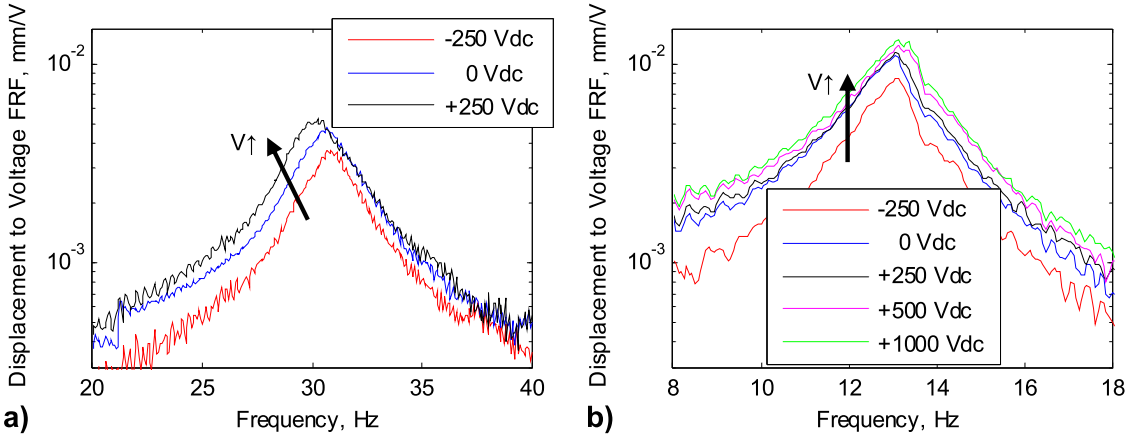

Figure 12. Single-point out-of-plane displacement to harmonic voltage excitation FRF of the bistable piezocomposite wing clamped to the base airfoil and mounted on the wind tunnel load balance: (a) *State 1* and (b) *State 2*. $V_{peak} = 200\ V_{ac}$.

a monostable wing. This effectively 'softening' behavior is expected since the MFC actuators are bonded to the lower surface of the wing. Increasing voltage causes them to induce a bending moment on the structure which moves the structure closer to the unstable equilibrium and hence towards *State 2*.

Similar to the above, figure 12(b) presents the frequency response around the first bending resonance of the bistable wing when it is in *State 2*, which is referred to as the compliant state. The resonance is observed around 13.1 Hz for the wing in *State 1* and excited with a −250 V_{dc} offset. The resonance frequencies for 0, +250, +500 and +1000 V_{dc} are also observed around 13.1 Hz. Note that the curvature induced with the MFC actuators with positive excitation voltages moves the wing towards the *State 2* and away from *State 1* stable equilibrium positions. In contrast to the relationship observed for *State 1*, a softening or hardening behavior is not observed as a function of DC offset and hence as a function of curvature. Such behavior, for the range of DC offset values examined here, is expected. Once the wing is in *State 2*, the chordwise curvature distribution along the spanwise direction is roughly zero (see table 1 and figure 9). Further changes in the spanwise curvature, induced by the MFC actuators, do not strongly couple into the chordwise curvature distribution; therefore the spanwise bending stiffness of the wing remains relatively fixed. Since the energy density of the MFC actuator is relatively limited, the observation above remains valid for the DC offset values that are attainable by the actuator.

The FRF tests that are presented above indicate the resonance frequencies for both states where a large amount of deformation can be achieved with a low excitation voltage. The tests also suggest that the DC offset values can be used to fine tune the dynamic behavior of the bistable wing. A set of discrete trials are conducted to see if snap-through can be achieved dynamically in the wind-off condition. Note that the MFC actuator has a recommended voltage range of −500 to +1500 V. Excitation voltages below −800 V_{dc} typically repolarize the PZT fibers. On the other hand, excitation voltages above +1800 V_{dc} typically result in shortages in the form of dielectric breakdown of the PZT material and/or the epoxy matrix. A combination of the AC (amplitude) and the DC (offset) excitation values are selected so that this range is not exceeded. In table 2, it is observed that snap-through from *State 1* to *State 2* can be achieved with a sinusoidal excitation with 800 V_{ac} amplitude at 29.9 Hz and with +250 V_{dc} offset. Higher excitation amplitudes will also result in snap-through. Snap-through from *State 2* to *State 1* can be achieved with a sinusoidal excitation with 700 V_{ac} amplitude at 13.1 Hz and with 0 V_{dc} offset. These initial observations in the wind-off condition will be used as a guide to determine the excitation parameters during the wind-on experiments which will be presented in section 4.5.

Table 2. Wind-off dynamic snap-through behavior of the bistable wing from two different stable equilibria.

State	DC offset (V_{dc})	Excitation frequency (Hz)	Is snap achieved for (V_{ac} values)?
1 to 2	−250	30.8	No (≤500)
	0	30.6	No (≤600)
	+250	**29.9**	**Yes (≈800)**
	+500	n/a	Yes (with small disturbance)
2 to 1	−250	13.1	No (≤500)
	0	**13.1**	**Yes (≈700)**
	+250	13.1	No (≤1000)
	+500	13.1	No (≤1000)
	+1000	13.1	No (≤700)

In addition to the dynamic excitation, the static excitation is also examined to determine if snap-through can be achieved. A test is conducted where the DC excitation is started from −700 V, in *State 1*, and increased to +1700 V. During the increasing portion of the test, a snap-through is observed in the +500 to +1000 V range in different trials. The variation of the snap-through voltage is due to the past history of the excitation (e.g. stresses stored in the memory of the structure due to hysteresis). Once a snap-through occurs from *State 1* to *State 2*, the structure is no longer bistable due to the static curvature induced by the MFC actuator. The test procedure is continued where the excitation is decreased from +1700 to −700 V. The specimen does become bistable as voltage is reduced; however, snap-through is not achievable,

Table 3. Wind-off static snap-through behavior of the bistable wing from two different stable equilibria.

DC offset (V_{dc})	Bistable?	Snap from 1 to 2? (for increasing V_{dc})	Snap from 2 to 1? (for decreasing V_{dc})
−700	Yes	No	No
−500	Yes	No	No
−250	Yes	No	No
0	Yes	No	No
+250	Yes	No	No
+500	**Transition**	**Yes (with small disturbance)**	**No**
+1000	**Transition**	**Yes (with small disturbance)**	**No**
+1250	No	Yes	No
+1500	No	Yes	No
+1700	No	Yes	No

with static excitation, from *State 2* to *State 1*. Table 3 presents the static snap-through behavior in detail.

An important observation is that, from the data given in tables 2 and 3, it appears that static excitation can achieve snap-through from *State 1* to *State 2* at a lower peak excitation value compared to dynamic excitation. This observed behavior is artificially caused by the wind tunnel and the load balance setup. As illustrated in figure 5, the complete wing structure which consists of the bistable wing and the base airfoil is connected to the load balance with a sting. The sting, from the load balance to the root of the base airfoil is 419 mm long; therefore the boundary condition effective to the base airfoil and the bistable wing in the wind tunnel is a combination of a soft translational spring and a stiff torsional spring. A dynamic excitation using the MFC actuator results in lower curvatures in the bistable wing because of the compliancy in the boundary condition in the wind tunnel. It is important to consider possible boundary conditions in most aircraft applications. Two common cases are possible: (1) the condition where the bistable wing structure has small inertia when compared to the rest of the wing or the fuselage; (2) the bistable wing has a symmetric twin and both structures are excited symmetrically. In both cases, which are structurally more realistic, the dynamic excitation will be superior to the static excitation in displacement-to-voltage-excitation performance.

4.5. Aerodynamic response of bistable wing—control on

The second aerodynamic measurement on the bistable wing is conducted to understand the actively induced snap-through that is caused due to the strain induced by the MFC actuator. Similar to the previous tests, a set of AOA sweeps are conducted in the range of 10–20 m s^{-1} nominal velocity values: the velocity range is swept in 2.5 m s^{-1} steps. The AOA sweep is conducted, in both directions, in the range of −20° to +20°: the AOA range is swept in 0.5° steps. The goal here is to demonstrate that the structure can be made, effectively, monostable against a certain level of adverse pressure gradient. This property, if demonstrated, shows the controllability of a desired state. The critical values of voltage excitation amplitude, frequency (and DC offset if necessary) are key values in determining the controllability properties.

First, the excitation parameters that induce snap-through from *State 2* to *State 1* are examined. A sinusoidal excitation with 800 V_{ac} amplitude at 13.0 Hz is applied which corresponds to the resonance frequency of *State 2*. This excitation causes the wing to be effectively monostable for *State 1*. Next, a fixed freestream velocity is selected and applied. The AOA is started at −20° where both the dynamic excitation and the pressure gradient are favorable to *State 1*. In addition, further increase in the magnitude (e.g. AOA $<-20°$) does not induce snap-through to *State 2*. The AOA is incremented in 0.5° steps. As the AOA is increased, the favorable pressure gradient to *State 1* switches, at an unknown value, to the adverse pressure gradient to *State 1*. The pressure gradient becomes favorable to *State 2*. Further increase in the AOA may cause the adverse pressure gradient to induce snap-through from *State 1* to *State 2* at a critical AOA value; however, this critical AOA value is reduced by the 'disturbance' of the sinusoidal excitation when compared to the passive wing. (In most applications, the resonant control method would be used to snap to a desired state and disabled when the desired state is reached.) The cycle is reversed when starting the AOA at +20° and reducing it to −20°. The snap-through from *State 2* to *State 1* will occur at a critical AOA value regardless of the net pressure because of the dynamic excitation. A critical freestream velocity still exists for a preselected range of AOA; however, this critical velocity value is lower than the one observed for the passive structure. Below the critical freestream velocity, *State 1* can be held for the entire AOA range that is of interest even in the presence of dynamic excitation tuned for the resonance of *State 2*. Figure 13 presents the aerodynamic response of the bistable plate at three different freestream velocities where the AOA is first swept up from −20° to +20° and swept back down to −20°. The path *abcdefa* is indicated in the figures to aid the discussion. The wing is set at *State 1* which is the favorable state at −20° AOA. As noted above, five velocity values are examined; however, only the three important velocity values are presented.

As before, the independent variable for the pitch angle is selected as the angle determined by the rotary table. Figure 13 also presents the theoretical finite-wing lift curve for reference and to aid comparison to the flat plate response. A snap-through is not observed for the complete AOA range, in either direction, at 13.2 m s^{-1} and all other velocities below this critical velocity value. Due to the lack of aerodynamic hysteresis, the AOA up and down sweeps are averaged and presented as a single curve for the 13.2 m s^{-1} velocity test. In contrast, at 15.5 and 17.8 m s^{-1}, snap-through is observed in both direction as expected—indicating that the critical velocity value is in the range of 13.2–15.5 m s^{-1}. (Note: if a gust causes the wing to go in to *State 2*, snap-through from *State 2* to *State 1* is always guaranteed for velocities below the critical velocity independent of the AOA). In contrast to the passive structure, a dynamically induced snap-through from *State 2* to 1 is observed near a mount angle of 0° where the pressure gradient is near neutral (see the path *ef* in

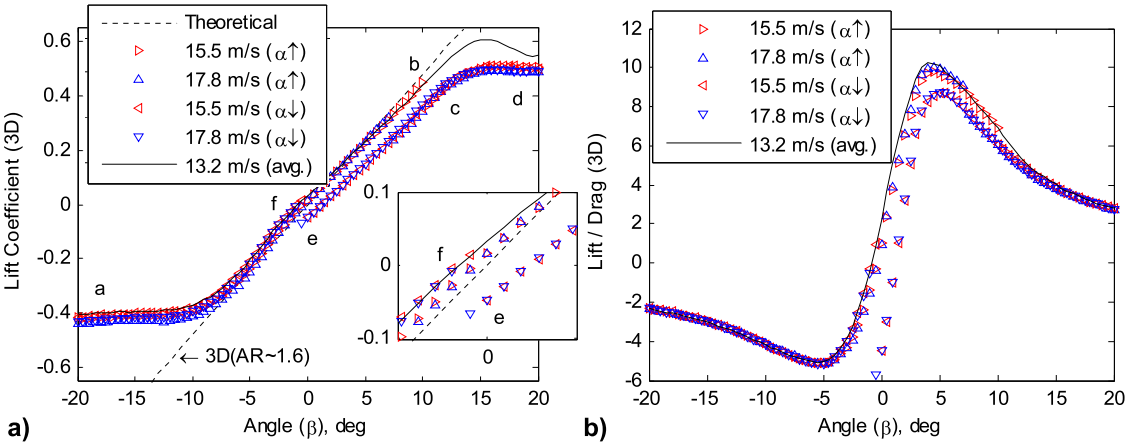

Figure 13. Experimental (3D) aerodynamic response of the active bistable wing to rotation angle sweep (up–down) and freestream velocity: (a) lift coefficient, (b) lift-to-drag ratio. $Re_{\mathrm{MAC}} = 162\,000$, 189 000 and 218 000. Sine tone excitation at 13.0 Hz, 800 V_{ac} amplitude and 0 V_{dc} offset.

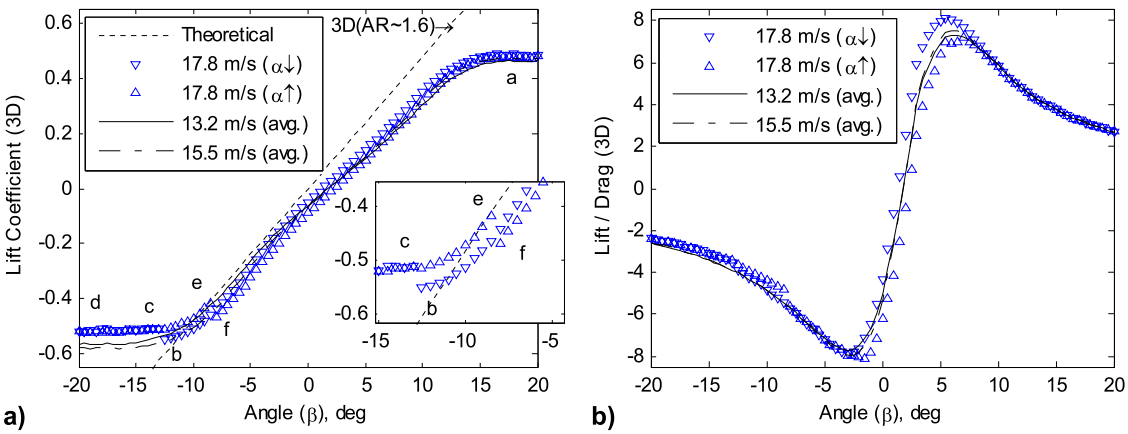

Figure 14. Experimental (3D) aerodynamic response of the active bistable wing to rotation angle sweep (down–up) and freestream velocity: (a) lift coefficient, (b) lift-to-drag ratio. $Re_{\mathrm{MAC}} = 162\,000$, 189 000 and 218 000. Sine tone excitation at 30.0 Hz, 1000 V_{ac} amplitude and 300 V_{dc} offset.

figure 13). The snap-through occurs at $-0.5°$ and $0.0°$ for the velocities of 17.8 and 15.5 m s^{-1} respectively indicating that the dynamic excitation can achieve snap-through from *State 2* to *State 1* by tailoring the composite and optimizing the distribution of actuation.

Similar to the discussion above, figure 14 presents the aerodynamic response of the dynamically excited bistable plate at three different freestream velocities where the AOA is first swept down from $+20°$ to $-20°$ and swept back up to $+20°$. The wing is set at *State 2* which is the favorable state at $+20°$. AOA due to pressure gradient and also favorable due to dynamic excitation at the resonance frequency of *State 1*. A sinusoidal excitation with 1000 V_{ac} amplitude at 30.0 Hz and 300 V_{dc} offset is applied—the excitation frequency is near the resonance frequency of *State 1*.

The response for the AOA down–up sweep is different from the previously presented AOA up–down sweep. A snap-through is not observed for the complete AOA range, in either direction, at 13.2 and 15.5 m s^{-1} and all other velocities below the value of 13.2 m s^{-1}. Due to the lack of aerodynamic hysteresis, the AOA up and down sweeps are averaged for the 13.2 and 15.5 m s^{-1} velocity tests. In contrast, at 17.8 m s^{-1}, snap-through is observed in both directions—indicating that the critical velocity value is in the range of 15.5–17.8 m s^{-1}. In the case where *State 2* is the desired state, the dynamic excitation is clearly capable of achieving *State 2* in the presence of adverse pressure gradient (see the path *ef* in figure 14) before it is triggered aerodynamically.

5. Conclusions

The aerodynamic evaluation of a dynamic control technique applied to a bistable composite plate with surface bonded piezoelectric actuators is presented. The prototype wing demonstrated sufficient passive bending stiffness and torsional rigidity to sustain its shape under aerodynamic loading while preserving the desired bistable behavior. By the use of the resonant control technique, the plate can be turned into an effectively monostable structure, or alternatively both stable equilibrium states can be reached both actively and passively from the other state. Dynamic forward and reverse

snap-through is demonstrated up to the maximum tested flow velocity of 20 m s^{-1} and in the AOA range of ±20° which shows both effectiveness of the piezoelectric actuation as well as the load carrying capability of both equilibrium states of the bistable wing.

Based on previous theoretical and bench-top evaluations by the authors as well as the current experimental aerodynamic examination, the authors believe the following conclusions can be drawn: (1) reversible dynamic snap-through is possible on a two- or four-ply unsymmetric laminate using surface bonded MFC actuators, (2) the composite structure is capable of carrying the aerodynamic loads through an aerodynamically desirable range of dynamic pressures, and (3) dynamic snap-through can be achieved against adverse pressure gradients. These conclusions prove the feasibility of the proposed concept for implementation in 'small-scale' aircraft operating in a low Reynolds number flow.

Acknowledgments

This work is supported by the European Research Council grant number 247045 entitled 'Optimization of Multi-scale Structures with Applications to Morphing Aircraft'. The authors would like to thank Professor Helmut Schürmann and Mr Hasan Dadak of the Fachgebiet Konstruktiver Leichtbau und Bauweisen (KLuB) group at the Technische Universität Darmstadt for their support in the manufacturing of the tested composite specimens.

References

[1] Sofla A Y N, Meguid S A, Tan K T and Yeo W K 2010 Shape morphing of aircraft wing: status and challenges *Mater. Des.* **31** 1284–92

[2] Barbarino S, Bilgen O, Ajaj R M, Friswell M I and Inman D J 2011 A review of morphing aircraft *J. Intell. Mater. Syst. Struct.* **22** 823–77

[3] Gomez J C and Garcia E 2011 Morphing unmanned aerial vehicles *Smart Mater. Struct.* **20** 103001

[4] Hyer M W 1981 Some observations on the cured shapes of thin unsymmetric laminates *J. Compos. Mater.* **15** 175–94

[5] Hyer M W 1981 Calculations of the room-temperature shapes of unsymmetric laminates *J. Compos. Mater.* **15** 296–310

[6] Arrieta A F, Neild S A and Wagg D J 2010 On the cross-well dynamics of a bi-stable composite plate *J. Sound Vib.* **330** 3424–41

[7] Eggleston G, Hutchison C, Johnston C, Koch B, Wargo G and Williams K 2002 *Morphing Aircraft Design Team, Virginia Tech Aerospace Engineering Senior Design Project*

[8] Barrett R M, Vos R, Tiso P and De Breuker R 2005 Post-Buckled Precompressed (PBP) actuators: enhancing VTOL autonomous high speed MAVs *46th AIAA/ASME/ASCE/AHS/ASC Structure, Structural Dynamics & Materials Conf. (Austin, TX)* AIAA 2005-2113

[9] Vos R, De Breuker R, Barrett R and Tiso P 2007 Morphing wing flight control via Post Buckled Precompressed piezoelectric actuators *J. Aircr.* **44** 1060–8

[10] Vos R, Barrett R and Zehr D 2008 Magnification of work output in PBP class actuators using buckling/converse buckling techniques *49th AIAA/ASME/ASCE/AHS/ASC Structures, Structural Dynamics, and Materials Conf. (Schaumburg, IL)* AIAA 2008-1705

[11] Kim D K and Han J H 2006 Smart flapping wing using Macro-Fiber Composite actuators *Proc. SPIE* **6173** 61730F

[12] Kim D K, Han J H and Kwon K J 2009 Wind tunnel tests for a flapping wing model with a changeable camber using Macro-Fiber Composite actuators *Smart Mater. Struct.* **18** 024008

[13] Bilgen O, Kochersberger K B, Diggs E C, Kurdila A J and Inman D J 2007 Morphing wing micro-air-vehicles via Macro-Fiber-Composite actuators *48th AIAA/ASME/ASCE/AHS/ASC Structures, Structural Dynamics, and Materials Conf. (Honolulu, HI)* AIAA-2007-1785

[14] Bilgen O, Kochersberger K B and Inman D J 2009 Macro-Fiber Composite actuators for a swept wing unmanned aircraft *Aeronaut. J.* **113** 385–95

[15] Bilgen O, Kochersberger K B, Inman D J and Ohanian O J 2010 Macro-Fiber Composite actuated simply-supported thin morphing airfoils *Smart Mater. Struct.* **19** 055010

[16] Bilgen O, Kochersberger K B, Inman D J and Ohanian O J 2010 Novel, bi-directional, variable camber airfoil via Macro-Fiber Composite actuators *J. Aircr.* **47** 303–14

[17] Paradies R and Ciresa P 2009 Active wing design with integrated flight control using piezoelectric macro fiber composites *Smart Mater. Struct.* **18** 035010

[18] Wickramasinghe V K, Chen Y, Martinez M, Kernaghan R and Wong F 2009 Design and verification of a smart wing for an extremely-agile micro-air-vehicle *50th AIAA/ASME/ASCE/AHS/ASC Structures, Structural Dynamics, and Materials Conf. (Palm Springs, CA)* AIAA 2009-2132

[19] Butt L, Day S, Sossi C, Weaver J, Wolek A, Bilgen O, Inman D J and Mason W H 2010 *Wing Morphing Design Team Final Report 2010* (Blacksburg, VA: Virginia Tech Departments of Mechanical Engineering and Aerospace and Ocean Engineering Senior Design Project)

[20] Butt L, Bilgen O, Day S, Sossi C, Weaver J, Wolek A, Inman D J and Mason W H 2010 Wing morphing design utilizing macro fiber composite *Society of Allied Weight Engineers (SAWE) 69th Annual Conf. (Virginia Beach, VA)* Paper Number 3515-S

[21] Bilgen O, Butt L M, Day S R, Sossi C A, Weaver J P, Wolek A, Mason W H and Inman D J 2011 A novel unmanned aircraft with solid-state control surfaces: analysis and flight demonstration *52nd AIAA/ASME/ASCE/AHS/ASC Structures, Structural Dynamics, and Materials (Denver, CO)*

[22] Bilgen O, Butt L M, Day S R, Sossi C A, Weaver J P, Wolek A, Mason W H and Inman D J 2012 A novel unmanned aircraft with solid-state control surfaces: analysis and flight demonstration *J. Intell. Mater. Syst. Struct.* **24** 147–67

[23] Ohanian O J, Hickling C, Stiltner B, Karni E D, Kochersberger K B, Probst T, Gelhausen P A and Blain A P 2012 Piezoelectric morphing versus servo-actuated MAV control surfaces *53rd AIAA/ASME/ASCE/AHS/ASC Structures, Structural Dynamics and Materials Conf. (Honolulu, HI)* AIAA 2012-1512

[24] Dano M L and Hyer M W 2003 Sma-induced snap-through of unsymmetric fiberreinforced composite laminates *Int. J. Solids Struct.* **40** 5949–72

[25] Schultz M R, Hyer M W, Williams R B, Wilkie W K and Inman D J 2006 Snap-through of unsymmetric laminates using piezocomposite actuators *Compos. Sci. Technol.* **66** 2442–8

[26] Mattioni F, Weaver P M and Friswell M I 2005 The application of multi-stable composites to morphing structures *ICAST: Int. Conf. on Adaptive Structures and Technologies (Paris)* pp 45–52

[27] Mattioni F, Weaver P M, Potter K D and Friswell M I 2008 The application of thermally induced multistable composites to morphing aircraft structures *SPIE Smart Structures and Materials & Nondestructive Evaluation and Health Monitoring* pp 6930–8
[28] Mattioni F 2009 Thermally induced multi-stable composites for morphing aircraft applications *PhD Dissertation* University of Bristol
[29] Diaconu C G, Weaver P M and Mattioni F 2008 Concepts for morphing airfoil sections using bistable laminated composite structures *Thin Walled Struct.* **46** 689–701
[30] Diaconu C G, Weaver P M and Arrieta A F 2009 Dynamic analysis of bistable composite plates *J. Sound Vib.* **22** 987–1004
[31] Daynes S, Weaver P M and Potter K D 2009 Aeroelastic study of bistable composite airfoils *J. Aircr.* **46** 2169–73
[32] Arrieta A F, Wagg D J and Neild S A 2011 Dynamic snap-through for morphing of bi-stable composite plates *J. Intell. Mater. Syst. Struct.* **22** 103–22
[33] Senba A, Ikeda T and Ueda T 2010 A two-way morphing actuation of bistable composites with piezoelectric fibers *51st AIAA/ASME/ASCE/AHS/ASC Structures, Structural Dynamics and Materials Conf.*
[34] Virgin L N 2007 *Vibration of Axially-Loaded Structures* (Cambridge: Cambridge University Press)
[35] Arrieta A F, Spelsberg-Korspeter G, Neild S A, Hagedorn P and Wagg D J 2011 Low order model for the dynamics of a bistable composite plate *J. Intell. Mater. Syst. Struct.* **22** 2025–43
[36] Vogl G A and Hyer M W 2011 Natural vibration of unsymmetric cross-ply laminates *J. Sound Vib.* **330** 4764–79
[37] Arrieta A F, Bilgen O, Friswell M I and Hagedorn P 2012 Dynamic control for morphing of bi-stable composites *J. Intell. Mater. Syst. Struct.* at press (special issue) doi:10.1177/1045389X12449918 published online
[38] Arrieta A F, Bilgen O, Friswell M I and Hagedorn P 2012 Passive load alleviation bi-stable morphing concept *AIP Adv.* **2** 032118
[39] Arrieta A F, Bilgen O, Friswell M I and Ermanni P 2013 Modelling and configuration control of wing-shaped bi-stable piezoelectric composites *Aerospace Sci. Technol.* submitted
[40] SLG 2011 *High-Performance Prepregs: Preimpregnated Products for Fiber-Reinforced Composites* SLG Group, The Carbon Company www.sglgroup.com
[41] Wilkie W K, Bryant G R and High J W 2000 Low-cost piezocomposite actuator for structural control applications *SPIE 7th Annual International Symposium on Smart Structures and Materials (Newport Beach, CA)*
[42] High J W and Wilkie W K 2003 *Method of Fabricating NASA-Standard Macro-Fiber Composite Piezoelectric Actuators* NASA/TM-2003-212427, ARL-TR-2833
[43] Hagood N W, Kindel R, Ghandi K and Gaudenzi P 1993 Improving transverse actuation using interdigitated surface electrodes *North American Conf. on Smart Structures and Materials (Albuquerque, NM)* SPIE Paper No. 1917–25, 341–352
[44] Bilgen O, Erturk A and Inman D J 2010 Analytical and experimental characterization of Macro-Fiber Composite actuated thin clamped-free unimorph benders *J. Vib. Acoust.* **132** 051005
[45] Mueller T J and Burns T F 1982 *Experimental Studies of the Eppler 61 Airfoil at Low Reynolds Numbers* AIAA Paper 82-0345
[46] Selig M S and McGranahan B D 2004 Wind tunnel aerodynamic tests of six airfoils for use on small wind turbines *Trans. ASME* **126** 986–1000
[47] Barlow J B, Rae W H Jr and Pope A 1999 *Low-Speed Wind Tunnel Testing* 3rd edn (New York: Wiley)
[48] Fox R W, McDonald A T and Pritchard P J 2004 *Introduction to Fluid Mechanics* 6th edn (New York: Wiley)
[49] AIAA 1995 *AIAA Standard on Assessment of Experimental Uncertainty with Application to Wind Tunnel Testing* S-071A-1995 (New York: AIAA)